R-matrix approach to low-energy electron energy-loss spectroscopy from NiO

P. Jones and J. E. Inglesfield
Department of Physics and Astronomy, University of Wales Cardiff, P.O. Box 913, Cardiff, CF24 3YB, United Kingdom

J. J. M. Michiels
CBS, Postbus 4481, NL-6401 CZ, Heerlen, Netherlands

C. J. Noble and V. M. Burke
Daresbury Laboratory, Daresbury, Warrington, WA4 4AD, United Kingdom

P. G. Burke
Department of Applied Mathematics and Theoretical Physics, Queen's University, Belfast, BT7 1NN, United Kingdom
(Received 3 July 2000)

Low-energy electron energy-loss spectra from NiO have been calculated using *R*-matrix methods to describe the excitation of $3d$-$3d$ transitions on the Ni ions. The effect of the crystal field is fully included, though only single scattering is considered at this stage. The total scattering cross sections demonstrate the importance of exchange-scattering processes in addition to direct scattering, even at higher energies of the scattering electron. The differential cross sections allow the investigation of angular, spin, and symmetry dependence for comparison with experiment. For certain transitions the angular dependence shows zeros associated with the point group symmetry of the Ni ion, and these are discussed. The ratio of spin-flip to non-spin-flip contributions is calculated exactly for multiplicity-changing transitions, and is shown to be independent of scattering geometry and energy of the incident electron.

I. INTRODUCTION

Electron energy-loss (EELS) experiments provide an important probe of the electronic structure of solids, yielding information on the momentum and energy transfer associated with electronic excitations.[1] At high primary energies this can be described in the Born approximation by a dielectric loss function.[2] Recently, there has been much interest in low-energy EELS (LE-EELS) in which electrons with a primary energy of typically 20–100 eV are scattered in low-energy electron diffraction (LEED) geometry–non-dipole-active transitions can be excited by impact scattering, and electron exchange can give rise to multiplicity-changing transitions.[3] LE-EELS has been used to study the localized $3d$-$3d$ intra-atomic excitations in transition-metal compounds, particularly interesting because they may play a role in high-temperature superconductivity. The loss energies measured in this way are well described by a parametrized crystal field model. However, the work described here and in a previous Letter[4] is the first attempt to explain the actual loss spectra and their dependence on primary energy, angle of scattering, and spin polarization. We use the *R*-matrix method from atomic physics,[5] generalizing it to the solid-state environment, and apply it to LE-EELS from NiO.[3,6]

The *R*-matrix method is a multichannel version of scattering theory, taking into account inelastic processes corresponding to excitations within the scattering center, which in our case is the Ni^{2+} ion. The central idea in *R*-matrix theory is that space is separated into two regions:[5] the inner region where the scattering electron fully interacts with the target, and an outer region where the now distinguishable electron moves in an effective field produced by the target system and its surroundings. Our modification of the method is to include the crystal field in which the Ni^{2+} ion is situated—this has a strong effect on the target and its interaction with the scattering electron. At this stage we only calculate single-site scattering, though in the final section of this paper we shall outline the inclusion of multiple scattering, which will be the subject of subsequent work.

After describing the *R*-matrix method in Sec. II, in Secs. III–V we shall explain how it is modified to include the effect of the octahedral crystal field appropriate to Ni^{2+} in NiO. A group theoretical analysis is needed, not only for identifying the different states, but also to factorize the Hamiltonian and the *R* matrix. A major part of the work is consequently the transformation between the spherical group and the octahedral O_h group. Another important modification compared with atomic physics applications of the *R*-matrix method is that we use a much smaller sphere radius separating the inner and outer regions, an atomic sphere radius of 2.58 a.u. compared with typically 7 a.u. in scattering from a free atom. In Sec. VI results will be given for total and differential cross sections as a function of primary electron energy, together with spin dependence of the scattering. This provides information on the relative importance of direct and exchange scattering. The relative strength of the various transitions will be explained, and a symmetry analysis will be used to discuss zeros in the differential cross sections in certain geometries. We shall compare our results with several experiments[3,6] in Sec. VII, and on the whole agreement will turn out to be satisfactory. Finally in Sec. VIII we shall discuss the extension to multiple-scattering theory.

II. *R*-MATRIX THEORY

R-matrix theory is widely used to solve electron-scattering problems in atomic and molecular physics.[7,8] We

shall now outline the theory as applied to electron scattering by a single-scattering atom or ion with N **active electrons.**

The $(N+1)$-electron Schrödinger equation that we wish to solve is

$$H_{N+1}\Psi = E\Psi. \tag{1}$$

The basic idea of R-matrix theory is the separation of the space surrounding the atom into two regions: an internal region ($r \leqslant a$) where the scattering electron interacts strongly with the target and in which we describe the many-electron system by a $(N+1)$-electron wave function, and an external region ($r > a$) where the scattered electron moves in an effective one-electron field produced by the target and its surroundings. In the internal region we build up the solution to Eq. (1) from $(N+1)$-electron basis functions, but before we can do this we make the Hamiltonian in this bounded region explicitly Hermitian by adding on the Bloch operator[9,10] defined over the R-matrix sphere

$$L_{N+1} = \sum_{i=1}^{N+1} \frac{1}{2}\delta(r_i - a)\left(\frac{\partial}{\partial r_i} - \frac{b-1}{r_i}\right). \tag{2}$$

Here r_i is the radial coordinate of the ith electron, and b is a constant that is conventionally introduced to provide some variational flexibility in the boundary condition. The $(N+1)$-electron basis functions used to expand Ψ in the internal region satisfy the matrix Schrödinger equation

$$\langle \psi_k | H_{N+1} + L_{N+1} | \psi_j \rangle_{\text{int}} = E_k \delta_{kj}, \tag{3}$$

where the integral in the matrix element is over the internal region only. The solutions to Eq. (3) satisfy the Schrödinger equation (1) within the internal region, with the following homogeneous boundary condition on the boundary:

$$\frac{1}{\psi_k}\frac{\partial(r\psi_k)}{\partial r_i} = b. \tag{4}$$

We shall take $b=0$ in this work. To find the full solution of the Schrödinger equation Ψ, matched onto the outer region, in terms of these basis functions we rewrite Eq. (1) as

$$(H_{N+1} + L_{N+1} - E)\Psi = L_{N+1}\Psi, \tag{5}$$

and then from the Green function corresponding to Eq. (3) we obtain

$$|\Psi\rangle = \sum_k |\psi_k\rangle \frac{1}{E_k - E}\langle \psi_k | L_{N+1} | \Psi \rangle. \tag{6}$$

The $(N+1)$-electron basis functions ψ_k are built up from the N-electron eigenstates of the target Hamiltonian H_N, corresponding to the atom without the scattering electron:

$$H_N \Phi_i = \epsilon_i \Phi_i. \tag{7}$$

The target states are coupled to symmetry-adapted angular and spin functions of the scattering electron to form channel functions $\overline{\Phi}_\iota(\mathbf{x}_1, \ldots, \mathbf{x}_N; \hat{\mathbf{r}}_{N+1}, \sigma_{N+1})$, where $\mathbf{x}_1, \ldots, \mathbf{x}_N$ are the spatial and spin coordinates of the target electrons, and $\hat{\mathbf{r}}_{N+1}$ and σ_{N+1} are the angular and spin components of the scattering electron, respectively. The particular target state, say i, and scattering angular momentum, say l, are subsumed in the Greek index ι, though sometimes we shall give them explicitly. The channel functions are eigenstates of the total spin angular momentum; they also transform according to some representation of the spatial symmetry group of the system—in the case of the free atom they are eigenstates of the total orbital angular momentum. The basis functions are then expanded in the form

$$\begin{aligned}\psi_k(\mathbf{x}_1, \ldots, \mathbf{x}_{N+1}) = \mathcal{A}\sum_{\iota j} & \overline{\Phi}_\iota(\mathbf{x}_1, \ldots, \mathbf{x}_N; \hat{\mathbf{r}}_{N+1}, \sigma_{N+1}) \\ & \times r_{N+1}^{-1} u_j(r_{N+1}) a_{\iota jk} \\ & + \sum_i \chi_i(\mathbf{x}_1, \ldots, \mathbf{x}_{N+1}) b_{ik},\end{aligned} \tag{8}$$

where $\mathcal{A}$ is the antisymmetrization operator. The one-electron radial functions u_j represent the motion of the scattered electron. They form a complete radial basis and are eigenstates of a static one-electron approximation to H_{N+1},

$$-\frac{1}{2}\frac{d^2 u_j}{dr^2} + \frac{l(l+1)}{2r^2}u_j(r) + U_0(r)u_j(r) = E_j^0 u_j(r), \tag{9}$$

with the following R-matrix boundary condition:

$$\frac{a}{u_j}\frac{du_j}{dr} = b. \tag{10}$$

Finally, the χ_i's are bound states of the $(N+1)$-electron system that vanish by the R-matrix boundary and are included to ensure completeness. From the basis functions ψ_k and their energies E_k we can then construct the Green function in Eq. (6).

The full $(N+1)$-electron wave function Ψ is now projected onto the channel functions to give one-electron radial functions $F_\iota(r)$:

$$F_\iota(r) = r\langle \overline{\Phi}_\iota | \Psi \rangle'. \tag{11}$$

The prime indicates that the integration is carried out over all electron space and spin coordinates, except the radial coordinate of the scattered electron. Substituting into Eq. (6) and putting r on the R-matrix boundary, we then obtain a generalized logarithmic derivative equation for the F_ι's,

$$F_\iota(a) = a\sum_\kappa R_{\iota\kappa}(E)\left.\frac{dF_\kappa}{dr}\right|_{r=a}, \tag{12}$$

where we have introduced the R-matrix defined on the boundary

$$R_{\iota\kappa}(E) = \frac{1}{2a}\sum_k \frac{w_{\iota k} w_{\kappa k}}{E_k - E}, \tag{13}$$

with

$$w_{\iota k} = a\langle \overline{\Phi}_\iota | \psi_k \rangle'_{r=a}. \tag{14}$$

Equations (12) and (13) give the required boundary conditions on the F_ι functions so that they match onto the solutions of the $(N+1)$-electron problem within the internal region. F_ι is just the one-electron wave function of the scattered electron when the target is in the corresponding target state and satisfies a one-electron Schrödinger equation in the external region. With this generalized logarithmic derivative, the scattering solution is fully defined, and from the form of the functions F_ι we can find the t matrix for use in scattering calculations.[11]

III. INCLUDING THE CRYSTAL FIELD

The Ni^{2+} ion in NiO is in a cubic environment, and crystal field theory may be used to find the electron states of the d^8 ion.[12] In this section we shall describe how the crystal field can be included in a scattering calculation: the original computer codes for calculating the target states, channel functions, and radial functions use the spherical symmetry of the free ion, and these must all be transformed into functions forming representations of the octahedral O_h symmetry group. This allows us to factorize both the N-electron and $(N+1)$-electron Hamiltonians, greatly reducing the computational effort.

A. Target states

We first consider the target states of the Ni^{2+} ion in the octahedral field, considering only states associated with $3d$-$3d$ excitations. The $3d^8$ configuration gives rise to five terms in the spherical environment of the free ion:

$$ {}^1S^e,\ {}^3P^e,\ {}^1D^e,\ {}^3F^e,\ {}^1G^e, $$

with ${}^3F^e$ as the ground state. The crystal field potential has the form[12]

$$ V_c(r,\theta,\phi)=\left(\frac{7}{12}\right)^{1/2}\beta r^4\left[Y_{40}(\theta,\phi)+\left(\frac{5}{14}\right)^{1/2}[Y_{44}(\theta,\phi)+Y_{4-4}(\theta,\phi)]\right]+V_M, \tag{15} $$

where V_M, the Madelung potential, is the electrostatic shift at the origin due to the neighboring ions,[13] and this splits the spherical terms as follows:[14,15]

$$ \begin{aligned} {}^1S^e &\rightarrow {}^1A_{1g}, \\ {}^3P^e &\rightarrow {}^3T_{1g}, \\ {}^1D^e &\rightarrow {}^1E_g+{}^1T_{2g}, \\ {}^3F^e &\rightarrow {}^3A_{2g}+{}^3T_{1g}+{}^3T_{2g}, \\ {}^1G^e &\rightarrow {}^1A_{1g}+{}^1E_g+{}^1T_{1g}+{}^1T_{2g}. \end{aligned} \tag{16} $$

The labeling of the states on the right indicates the irreducible representation of O_h—A_1, A_2, E, T_1, or T_2—to which they belong. Note here that all states are even (g or gerade) since we are dealing with the case of two d holes for which the product wave function is always even. Forming the direct product

$$ d^e\otimes d^e\rightarrow S^e\oplus P^e\oplus D^e\oplus F^e\oplus G^e, \tag{17} $$

we see that all the states produced must be even.[16,12] In our scattering calculation we include these 11 target states, Eq. (16).

The five spherical target states are found from a Hartree-Fock calculation of free Ni^{2+}, with Hamiltonian H_N^0:

$$ \Phi_1={}^1S^e,\quad \Phi_2={}^3P^e,\quad \Phi_3={}^1D^e,\quad \Phi_4={}^3F^e,\quad \Phi_5={}^1G^e. \tag{18} $$

To find the 11 cubic target states we first form linear combinations of the spherical states that transform according to the different irreducible representations

$$ \begin{aligned} {}^1A_{1g}:&\quad \begin{cases} \tilde{\phi}_1=\Phi_1, \\ \tilde{\phi}_2=\sum_m b_{2m}\Phi_{5m}, \end{cases} \\ {}^3A_{2g}:&\quad \tilde{\phi}_3=\sum_m b_{3m}\Phi_{4m}, \\ {}^1E_g:&\quad \begin{cases} \tilde{\phi}_{4\mu}=\sum_m b_{4m}^{\mu}\Phi_{3m}, \\ \tilde{\phi}_{5\mu}=\sum_m b_{5m}^{\mu}\Phi_{5m}, \end{cases} \\ {}^1T_{1g}:&\quad \tilde{\phi}_{6\mu}=\sum_m b_{6m}^{\mu}\Phi_{5m}, \\ {}^3T_{1g}:&\quad \begin{cases} \tilde{\phi}_{7\mu}=\sum_m b_{7m}^{\mu}\Phi_{2m}, \\ \tilde{\phi}_{8\mu}=\sum_m b_{8m}^{\mu}\Phi_{4m}, \end{cases} \\ {}^1T_{2g}:&\quad \begin{cases} \tilde{\phi}_{9\mu}=\sum_m b_{9m}^{\mu}\Phi_{3m}, \\ \tilde{\phi}_{10\mu}=\sum_m b_{10m}^{\mu}\Phi_{5m}, \end{cases} \\ {}^3T_{2g}:&\quad \tilde{\phi}_{11\mu}=\sum_m b_{11m}^{\mu}\Phi_{4m}. \end{aligned} \tag{19} $$

The summations are over the magnetic quantum number m of the spherical states; in the case of two-dimensional E and three-dimensional T_1 and T_2, μ runs over the components of the representation. The tilde over the wave functions indicates cubic symmetry; b's are transformation coefficients found from group theoretical projection operator techniques.[14]

Linear combinations of the $\tilde{\phi}_k$'s with a particular spin and cubic symmetry give the target states $\tilde{\Phi}_{ip\mu}$. Here i numbers the state (1 to 11), p is the irreducible representation to which it belongs, and μ is the component of the representation. The linear combinations and target energies are found by diagonalizing the N-electron Hamiltonian

$$ H_N=H_N^0+V_c, \tag{20} $$

TABLE I. Ground state and excited states of $3d$-$3d$ excitations in NiO. The excitation energies are from the EELS experiments (Ref. 3) and are compared with our crystal field results. Energies are in eV.

Symmetry	EELS	Theory
$^3A_{2g}$	0.00	0.00
$^3T_{2g}$	1.10	1.05
^1E_g	1.60	1.70
$^3T_{1g}$	1.70	1.75
$^1T_{2g}$	2.75	2.70
$^1A_{1g}$	2.81	2.80
$^3T_{1g}$	3.00	3.13
$^1T_{1g}$	3.55	3.28
^1E_g	–	4.06
$^1T_{2g}$	–	4.12
$^1A_{1g}$	–	7.04

in the space of the $\tilde{\phi}_k$'s. Combining these linear combinations with the b's in Eq. (19) we can then write the cubic target states in terms of the spherical target states Φ_{km_k},

$$\tilde{\Phi}_{ip\mu}=\sum_{km_k} d_{ip\mu km_k}\Phi_{km_k}, \tag{21}$$

where $k=1,\ldots,5$.

In the spherical Hartree-Fock part of the problem involving H_N^0, we scale the electron-electron interaction by a factor of 0.7—this is a standard procedure in crystal field studies and represents the effects of hybridization of the d electrons with the ligand orbitals.[17,18] In the crystal field part of the problem, we cut the potential V_c off at a radius of 2.58 a.u., the atomic sphere radius of Ni in NiO as used in conventional band-structure calculations. (We shall subsequently evaluate the R-matrix at this radius.) Finally the N-electron excitation energies are known from the LE-EELS experiments,[3] and we use these to fix the strength parameter β in the crystal field potential (15). Taking $\beta=0.0418$ a.u. we obtain the excitation energies shown in Table I, in excellent agreement with experiment. The Madelung term in Eq. (15) will be treated in Sec. IV.

B. Channel functions

The $(N+1)$-electron scattering wave functions have one of the following 20 symmetries:

$$^2A_{1g/u},\ ^4A_{1g/u},\ ^2A_{2g/u},\ ^4A_{2g/u},\ ^2E_{g/u},$$

$$^4E_{g/u},\ ^2T_{1g/u},\ ^4T_{1g/u},\ ^2T_{2g/u},\ ^4T_{2g/u},$$

formed by combining a scattering electron with even (g) or odd (u) parity with the even target states. These symmetries also classify the channel functions $\tilde{\bar{\Phi}}$ and $(N+1)$-electron basis functions $\tilde{\psi}$ [Eq. (8)].

To form the channel functions we couple the cubic target states with angular and spin functions for the scattering electron. The spin functions we write as $\chi_{(1/2)m}(\sigma_{N+1})$. The angular functions appropriate to cubic symmetry are constructed from spherical harmonics

$$X_{hl}^{p\mu}(\hat{\mathbf{r}}_{N+1})=\sum_m b_{hlm}^{p\mu}Y_{lm}(\hat{\mathbf{r}}_{N+1}). \tag{22}$$

Once again p is the irreducible representation and μ its component; h labels the different possible linear combinations of the spherical harmonic with angular momentum l that transform like p. The b coefficients are the same as in Eq. (19) and are independent of parity, though we have written them with more labels in Eq. (22). This is not a trivial point, as from Eq. (17) all the spherical target states in Eq. (19), including $^3P^e$ and $^3F^e$, have even parity, whereas the odd l spherical harmonics in Eq. (22) have odd parity. We shall return to this point in a subsequent paper when we deal with scattering from an ion in tetragonal symmetry, where the situation is more complicated.

The cubic channel functions are then given by

$$\tilde{\bar{\Phi}}_{ip_1p_2hl}^{\tilde{\Gamma}}(\mathbf{x}_1,\ldots,\mathbf{x}_N;\hat{\mathbf{r}}_{N+1},\sigma_{N+1})$$

$$=\sum_{\mu_1\mu_2M_{S_i}m}(p_1\mu_1p_2\mu_2|PM_P)(S_iM_{S_i}\tfrac{1}{2}m|SM_S)$$

$$\times\tilde{\Phi}_{ip_1\mu_1}(\mathbf{x}_1,\ldots,\mathbf{x}_N)X_{hl}^{p_2\mu_2}(\hat{\mathbf{r}}_{N+1})\chi_{(1/2)m}(\sigma_{N+1}). \tag{23}$$

Here $(p_1\mu_1p_2\mu_2|PM_P)$ is the cubic Clebsch-Gordan coefficient that couples irreducible representations $p_1\mu_1$ and $p_2\mu_2$ to form PM_P, the irreducible representation and its component to which the channel function belongs; likewise $(S_iM_{S_i}\frac{1}{2}m|SM_S)$ is the Clebsch-Gordan coefficient that couples the spin $S_iM_{S_i}$ of the target state with the spin of the scattering electron to give the spin SM_S of the channel function. The superscript $\tilde{\Gamma}$ of the cubic channel function represents all the conserved quantum numbers,

$$\tilde{\Gamma}\equiv PM_P,\ SM_S,\ \Pi,$$

the irreducible representation, spin, and parity. The subscripts on the channel function give the target state (i), its symmetry (p_1), and the symmetry (p_2), branch (h), and angular momentum (l) of the scattering electron.

The cubic channel functions can be rewritten in terms of spherical channel functions $\bar{\Phi}_{kl}^{\Gamma}$, where k labels the target state from which the channel function is constructed, l is the angular momentum of the scattering electron, and Γ are the spherical quantum numbers

$$\Gamma\equiv LM_L,\ SM_S,\ \Pi,$$

the total orbital angular momentum, and the same spin and parity as in $\tilde{\Gamma}$. Substituting from Eq. (21) to replace the cubic target states by spherical target states, and from Eq. (22) to replace the $X_{hl}^{p_2\mu_2}$ by spherical harmonics, it can be shown that

$$\tilde{\bar{\Phi}}_{ip_1p_2hl}^{\tilde{\Gamma}}=\sum_{kLM_L}A_{ip_1p_2hkl}^{\tilde{\Gamma}\Gamma}\bar{\Phi}_{kl}^{\Gamma}, \tag{24}$$

where

$$A^{\tilde{\Gamma}\Gamma}_{ip_1p_2hkl} = \sum_{\mu_1\mu_2 m_k m} (p_1\mu_1 p_2\mu_2|PM_P) \times (l_k m_k lm|LM_L) d_{ip_1\mu_1 k m_k} b^{p_2\mu_2}_{hlm}. \quad (25)$$

This transformation is very useful for evaluating the matrix elements of the $(N+1)$-electron Hamiltonian, to which we now turn.

C. Matrix elements

The next stage in constructing the R matrix is to find the eigenstates $\tilde{\psi}^{\tilde{\Gamma}}_k$ of the $(N+1)$-electron Hamiltonian [Eq. (3) plus the crystal field]. The Hamiltonian factorizes into the different irreducible representations of the cubic group. Exactly as in Eq. (8), the $\tilde{\psi}^{\tilde{\Gamma}}_k$'s are expanded in terms of the antisymmetrized products of channel functions [Eqs. (23) and (24)] with the set of one-electron radial functions u_j together with bound states of the $(N+1)$-electron system:

$$\tilde{\psi}^{\tilde{\Gamma}}_k(\mathbf{x}_1,\ldots,\mathbf{x}_{N+1}) = \mathcal{A} \sum_{ip_1p_2hlj} \bar{\bar{\Phi}}^{\tilde{\Gamma}}_{ip_1p_2hl} \times (\mathbf{x}_1,\ldots,\mathbf{x}_N;\hat{\mathbf{r}}_{N+1},\sigma_{N+1}) \times r^{-1}_{N+1} u_j(r_{N+1}) a_{ip_1p_2hljk} + \sum_i \tilde{\chi}^{\tilde{\Gamma}}_i(\mathbf{x}_1,\ldots,\mathbf{x}_{N+1}) b_{ik}. \quad (26)$$

The states in the first summation are called continuum functions, because they are finite at the R-matrix boundary and match on to the scattering electron at the boundary. The bound states in the second summation come from the d^9 configuration of Ni^+; the spherical bound state has $^2D^e$ symmetry, which splits into ^2E_g and $^2T_{2g}$ in the cubic field. It is again convenient to write these in terms of the spherical bound state

$$\tilde{\chi}^{\tilde{\Gamma}}_i = \sum_m b^{PM_P}_{hlm} \chi_{lm}, \quad (27)$$

where $i=1,2$ labels the cubic states. The b coefficients are the same as in Eq. (22), with $h=1$ (only one linear combination of the spherical states occurs for each cubic irreducible representation in this case) and $l=2$ for the spherical angular momentum.

We now evaluate the matrix elements of the Hamiltonian, first the continuum-continuum matrix elements of the spherical part of the Hamiltonian H^0_{N+1}, including the Bloch operator

$$\tilde{H}^{0\tilde{\Gamma}}_{ip_1p_2hlj,i'p'_1p'_2h'l'j'} = \langle \mathcal{A}\bar{\bar{\Phi}}^{\tilde{\Gamma}}_{ip_1p_2hl} r^{-1}_{N+1} u_j | H^0_{N+1} | \mathcal{A}\bar{\bar{\Phi}}^{\tilde{\Gamma}}_{i'p'_1p'_2h'l'} r^{-1}_{N+1} u_{j'} \rangle. \quad (28)$$

Using Eq. (25) this can be related to the matrix elements between spherical states:

$$\tilde{H}^{0\tilde{\Gamma}}_{ip_1p_2hlj,i'p'_1p'_2h'l'j'} = \sum_{kk'LM_L} A^{\tilde{\Gamma}\Gamma}_{ip_1p_2hkl} \times A^{\tilde{\Gamma}\Gamma}_{i'p'_1p'_2h'k'l'} H^{0\Gamma}_{klj,k'l'j'}, \quad (29)$$

where

$$H^{0\Gamma}_{klj,k'l'j'} = \langle \mathcal{A}\bar{\Phi}^{\Gamma}_{kl} r^{-1}_{N+1} u_j | H^0_{N+1} | \mathcal{A}\bar{\Phi}^{\Gamma}_{k'l'} r^{-1}_{N+1} u_{j'} \rangle. \quad (30)$$

These spherical matrix elements can be calculated using a standard R-matrix code for electron-atom and electron-ion scattering.[19] Hence the matrix elements (28) are easily evaluated. As in the case of the target states (Sec. III A), the electron-electron interaction is scaled by 0.7.

The matrix elements of the crystal field (15) are also transformed to matrix elements between spherical states:

$$\tilde{V}^{\tilde{\Gamma}}_{cip_1p_2hlj,i'p'_1p'_2h'l'j'} = \sum_{kk'LM_LL'M'_L} A^{\tilde{\Gamma}\Gamma}_{ip_1p_2hkl} \times A^{\tilde{\Gamma}\Gamma'}_{i'p'_1p'_2h'k'l'} V^{\Gamma\Gamma'}_{cklj,k'l'j'}. \quad (31)$$

The spherical matrix elements

$$V^{\Gamma\Gamma'}_{cklj,k'l'j'} = \left\langle \mathcal{A}\bar{\Phi}^{\Gamma}_{kl} r^{-1}_{N+1} u_j \left| \sum_{i=1}^{N+1} V_c(r_i,\theta_i,\phi_i) \right| \mathcal{A}\bar{\Phi}^{\Gamma'}_{k'l'} r^{-1}_{N+1} u_{j'} \right\rangle \quad (32)$$

can be expressed in terms of the reduced matrix elements of r^4 using the Wigner-Eckart theorem,[14] which are also calculated by the standard R-matrix electron scattering code.[19]

In the case of ^2E_g and $^2T_{2g}$ symmetries, to which the bound state contributes, the continuum-bound and bound-bound matrix elements also have to be determined. These can also be found in terms of the corresponding spherical matrix elements, using Eqs. (25) and (27).

IV. *R* MATRIX AND SCATTERING IN THE CRYSTAL FIELD

Having diagonalized the $(N+1)$-electron Hamiltonian to give the eigenstates $\tilde{\psi}^{\tilde{\Gamma}}_k$ and the corresponding eigenvalues, we construct the R matrix. The R matrix is diagonal in the symmetry labels $\tilde{\Gamma}$, and each symmetry can be treated separately both for evaluating the R matrix and for calculating its contribution to the scattering.

Constructing the *R* matrix

The R matrix is given by the sum over states (13); the surface amplitudes in this summation (14) are given in terms of the expansion coefficients in Eq. (26):

$$w_{\iota k} = a\langle \bar{\bar{\Phi}}^{\tilde{\Gamma}}_{ip_1p_2hl} | \tilde{\psi}^{\tilde{\Gamma}}_k \rangle'_{r=a} = \sum_j u_j(a) a_{ip_1p_2hljk}. \quad (33)$$

(The channel index ι on w subsumes the labels ip_1p_2hlk.)

Now the sum over states is in principle over an infinite number of states—only then does it give the R matrix exactly. Needless to say, in practice the summation is finite, but fortunately the contribution from the omitted states can be approximated by the Buttle correction.[20] The idea of this is that the omitted states, which have higher energy, are relatively insensitive to the exact details of the potential and to many-body interactions with the target states. Their contribution to the R matrix can then be replaced by that of solutions to the static one-electron equation (9). Let us work with u_j's that satisfy a zero-derivative boundary condition at the R-matrix boundary, that is, Eq. (4) with $b=0$. The exact R matrix for the one-electron problem is then given by

$$R(E)=\frac{1}{2a}\sum_{j=1}^{\infty}\frac{u_j(a)^2}{E_j^0-E}. \tag{34}$$

But using Eq. (12) we can find the R matrix at energy E directly, from the solution to Eq. (9) at E integrated outwards to $r=a$:

$$R(E)=\frac{1}{a}\frac{u}{du/dr}\bigg|_{r=a}. \tag{35}$$

If we now consider a restricted summation over $\mathcal{N}$ eigenstates u_j in Eq. (34), the contribution to R from the missing eigenstates is given by

$$\frac{1}{2a}\sum_{j=\mathcal{N}+1}^{\infty}\frac{u_j(a)^2}{E_j^0-E}=\frac{1}{a}\frac{u}{du/dr}\bigg|_{r=a}-\frac{1}{2a}\sum_{j=1}^{\mathcal{N}}\frac{u_j(a)^2}{E_j^0-E}. \tag{36}$$

This is the Buttle correction, and by construction it provides an exact correction to the restricted sum of states for the static one-electron problem. Provided that $E_{\mathcal{N}}^0$ is big enough for the static Hamiltonian to provide a reasonable approximation to H_{N+1}, it may be added on to the summation (13) over the eigenstates of the $(N+1)$-electron Hamiltonian, found using $\mathcal{N}$ u_j's in Eq. (26), to correct for the missing states.

The radius a of the R-matrix sphere should in principle extend further than the target states and bound states in the expansions (8) and (26), and typically for the Ni^{2+} ion in free space $a=7$ a.u. However, in the solid-state environment an electron ''feels'' the full Coulomb potential of the ion over a much shorter distance, typically the atomic sphere radius, and beyond this radius it interacts predominantly with neighboring atoms. This is the muffin-tin or atomic sphere approximation that is frequently made in band-structure[21] and electron-molecule scattering calculations.[22] Of course there will still be some Coulomb interaction with the distant ion, that can mediate inelastic processes, but this will be screened by the intervening ions. The atomic sphere radius of Ni^{2+} in NiO is taken to be 2.58 a.u. from a conventional band-structure calculation,[23] and we determine the scattering at this radius. In a full multiple-scattering calculation we would consider scattering by all the atomic spheres in the crystal, but in this paper we use a single-scattering approximation, taking a constant potential outside the atomic sphere radius.

To evaluate the scattering at the smaller radius, we propagate the R matrix for Ni^{2+} back from 7 a.u. with the same one-electron effective Hamiltonian (9) used to find the u_j's. The R matrix at the larger radius provides the one-point logarithmic derivative boundary condition for integrating the Schrödinger equation backwards at the working energy E to the smaller radius. This integration is conveniently performed using standard R-matrix propagator techniques in which the range $2.58\ \text{a.u.}\leqslant r\leqslant 7$ a.u. is divided into sectors, $\{r_i\}$. R matrices at successively smaller radii are determined from the propagation equations

$$-r_iR(r_i)=G_{LL}^i-G_{LR}^i[G_{RR}^i-r_{i+1}R(r_{i+1})]^{-1}G_{RL}^i, \tag{37}$$

where the G^i are Green's functions corresponding to Eq. (9) evaluated on the left (L) or right (R) ith sector boundaries.[24] In the simplest model, which we use, the potential is represented as the sum of the spherical part of the static potential of the Ni^{2+} ion and an equivalent exchange potential of the form

$$V_E(r)\sim\frac{1}{4\pi}\rho(r)^{1/3}, \tag{38}$$

where ρ is the ground-state target density.[25] These are expected to provide an accurate representation of the full interaction in the outer part of the R-matrix internal region. In this case the single-electron-scattering equations (37) are uncoupled and it is possible to simplify the propagation scheme. Generalizations in which the equations are coupled by the full static potential are straightforward. At this point the solutions of the Schrödinger equation and their derivatives are then used to find the shifted R matrix (12).

The propagated R matrix gives the logarithmic derivative (12) of the scattering wave functions at this smaller radius a, and this completely defines the scattering properties. Beyond a we take a flat potential, and the outer region can be expanded in partial waves, labeled by the channel index, with radial dependence given by

$$F_{\iota\kappa}(r)=\hat{j}_\iota(p_\iota r)\,\delta_{\iota\kappa}+\hat{n}_\iota(p_\iota r)K_{\iota\kappa}, \tag{39}$$

where $\hat{j}_\iota$ and $\hat{n}_\iota$ are Riccati-Bessel functions, $K_{\iota\kappa}$ is the K matrix, and ι and κ run over the open channels. The momentum p_ι is given by

$$p_\iota^2+\epsilon_i=2E, \tag{40}$$

where ϵ_i is the energy of target state i associated with channel ι and E is the energy of the $(N+1)$-electron state. K can be found in terms of the R matrix using the matching equation (12):

$$\hat{j}(pa)+\hat{n}(pa)K=Ra\left(\frac{d\hat{j}(pr)}{dr}\bigg|_{r=a}+\frac{d\hat{n}(pr)}{dr}\bigg|_{r=a}K\right). \tag{41}$$

The scattering cross sections can be found from the on-shell t matrix, which describes the transition between a state in which the scattering electron has momentum $\mathbf{p}$ and the target is in state i and the state $\mathbf{p}',i'$

$$\langle \mathbf{p}',i'|t|\mathbf{p},i\rangle. \tag{42}$$

The t matrix is calculated from the K matrix defined in Eq. (39) by the equation

$$t=\frac{2iK}{1-iK}. \tag{43}$$

We shall show how the t matrix is used in Sec. V.

The Madelung potential V_M in the crystal field (15) is incorporated into the calculation as a shift in the discrete $(N+1)$-electron energies E_k in the R-matrix summation (13). Each E_k is shifted by

$$E_k \rightarrow E_k+(N+1)V_M, \tag{44}$$

but the target energies entering Eq. (40) are also shifted, giving a shift in the total energy

$$E \rightarrow E+NV_M. \tag{45}$$

The R matrix is then given by

$$R_{\iota\kappa}(E)=\frac{1}{2a}\sum_k \frac{w_{\iota k}w_{\kappa k}}{E_k+V_M-E}. \tag{46}$$

A charge of ± 2 on each ion in the NiO structure gives a value for V_M of $+0.87$ a.u. As the charge on the ions is certainly less than the nominal charge, we somewhat arbitrarily reduce V_M to $+0.75$ a.u. There is another potential shift in the problem—the inner potential, which gives a different zero of energy inside and outside the crystal. This shifts the scattering electron kinetic energy, but we neglect this effect. Our approximate treatment of these energy shifts is justified, we believe, by the relative insensitivity of our scattering results to primary electron energy.

V. SCATTERING CROSS SECTIONS

The scattering amplitude, for scattering an electron with momentum $\mathbf{p}$ and with the target in state i, to momentum $\mathbf{p}'$ and target i', is given in terms of the corresponding t matrix by[11]

$$f(\mathbf{p}',i'\leftarrow\mathbf{p},i)=-(2\pi)^2\langle \mathbf{p}',i'|t|\mathbf{p},i\rangle, \tag{47}$$

and the differential scattering cross section is then given by

$$\frac{d\sigma}{d\Omega}(\mathbf{p}',i'\leftarrow\mathbf{p},i)=\frac{p'}{p}|f(\mathbf{p}',i'\leftarrow\mathbf{p},i)|^2. \tag{48}$$

We now introduce a complete set of states in an angular momentum representation for the scattering electron:

$$\int dE\sum_i\sum_L |E,L,i\rangle\langle E,L,i|=1. \tag{49}$$

Here $|E,L,i\rangle$ corresponds to a spherical wave with angular momentum L incident on target i, with total energy E given by Eq. (40). Using Eq. (49), Eq. (47) becomes

$$\begin{aligned} f(\mathbf{p}',i'\leftarrow\mathbf{p},i)=&-(2\pi)^2\sum_{i''i'''}\sum_{L''L'''}\int dE''\int dE''' \\ &\times\langle \mathbf{p}',i'|E'',L'',i'\rangle \\ &\times\langle E'',L'',i''|t|E''',L''',i'''\rangle\langle E''',L''',i'''|\mathbf{p},i\rangle. \end{aligned} \tag{50}$$

Now

$$\langle E,L,i|\mathbf{p},i\rangle=\frac{1}{\sqrt{p}}\delta\left(E-\left(\frac{p^2}{2}+\epsilon_i\right)\right)Y_L(\hat{\mathbf{p}}), \tag{51}$$

and substituting into Eq. (50) and evaluating the integrals, we obtain

$$\begin{aligned} &f(\mathbf{p}',i'\leftarrow\mathbf{p},i) \\ &\quad=\frac{-(2\pi)^2}{\sqrt{pp'}}\sum_{LL'}\langle E,L',i'|t|E,L,i\rangle Y_L(\hat{\mathbf{p}})Y^*_{L'}(\hat{\mathbf{p}}'). \end{aligned} \tag{52}$$

Substituting back into Eq. (48) gives

$$\begin{aligned} &\frac{d\sigma}{d\Omega}(\mathbf{p}',i'\leftarrow\mathbf{p},i) \\ &\quad=\frac{(2\pi)^4}{p^2}\sum_{LL'}\sum_{L''L'''}\langle L',i'|t|L,i\rangle \\ &\qquad\times\langle L'',i|t^\dagger|L''',i'\rangle Y_L(\hat{\mathbf{p}})Y^*_{L''}(\hat{\mathbf{p}})Y^*_{L'}(\hat{\mathbf{p}}')Y_{L'''}(\hat{\mathbf{p}}'). \end{aligned} \tag{53}$$

We now convert the angular momentum representation $|L,i\rangle$ to our symmetry-adapted functions. This state is given explicitly by

$$|L,i\rangle=\tilde{\Phi}_{ip_1\mu_1}Y_{lm_l}\chi_{(1/2)\,m}, \tag{54}$$

and using Eqs. (22) and (23) and rearranging in terms of the channel function $\tilde{\Phi}^{PM_PSM_S\Pi}_{ip_1p_2hl}$ we obtain

$$\begin{aligned} |L,i\rangle=&\sum_{PM_PSM_S}\sum_{p_2\mu_2h}b^{*p_2\mu_2}_{hlm_l}(PM_P|p_1\mu_1p_2\mu_2) \\ &\times(SM_S|S_iM_{S_i\frac{1}{2}}m)\tilde{\Phi}^{PM_PSM_S\Pi}_{ip_1p_2hl}, \end{aligned} \tag{55}$$

where the coefficients in the summations have been defined previously. Substituting Eq. (55) into Eq. (53) and rearranging, we obtain the following expresssion for the differential scattering cross section:

$$\frac{d\sigma}{d\Omega}(\mathbf{p}'i'm'\leftarrow\mathbf{p}im)=\frac{(2\pi)^4}{p^2}\frac{1}{n_\alpha}\sum_{PSM_P}\sum_{P'S'M'_P}\sum_{p_2hl}\sum_{p'_2h'l'}\sum_{p''_2h''l''}\sum_{p'''_2h'''l'''}\langle\tilde{\bar{\Phi}}^{\tilde{\Gamma}}_{i'p'_1p'_2h'l'}|t|\tilde{\bar{\Phi}}^{\tilde{\Gamma}}_{ip_1p_2hl}\rangle\langle\tilde{\bar{\Phi}}^{\tilde{\Gamma}'}_{i'p'_1p'''_2h'''l'''}|t|\tilde{\bar{\Phi}}^{\tilde{\Gamma}'}_{ip_1p''_2h''l''}\rangle^*$$
$$\times\sum_{M_SM'_S}\sum_{M_{S_i}M'_{S_i}}\left(SM_S\middle|S_iM_{S_i}\frac{1}{2}m\right)\left(S'M'_S\middle|S_iM_{S_i}\frac{1}{2}m\right)\left(SM_S\middle|S'_iM'_{S_i}\frac{1}{2}m'\right)\left(S'M'_S\middle|S'_iM'_{S_i}\frac{1}{2}m'\right)$$
$$\times\left\{\begin{array}{c}p_2hl\\p''_2h''l''\\PM_PP'M'_P\end{array}\right\}_{\mathbf{p}}\left\{\begin{array}{c}p'_2h'l'\\p'''_2h'''l'''\\PM_PP'M'_P\end{array}\right\}_{\mathbf{p}'}, \tag{56}$$

where $\tilde{\Gamma}\equiv\{PS\Pi\}$. Here n_α is the degeneracy of the incoming channel and is given by $(2S_i+1)\times 2$. The curly brackets in this equation represent the following expression,

$$\left\{\begin{array}{c}p_2hl\\p''_2h''l''\\PM_PP'M'_P\end{array}\right\}_{\mathbf{p}}=\sum_{\mu'_2\mu''_2}\left(\sum_{m_l}b^{*p_2\mu_2}_{hlm_l}Y_{lm_l}(\hat{\mathbf{p}})\right)\left(\sum_{\mu_1}(PM_P|p_1\mu_1p_2\mu_2)(P'M'_P|p_1\mu_1p''_2\mu''_2)\right)\left(\sum_{m''_l}b^{p''_2\mu''_2}_{h''l''m''_l}Y^*_{l''m''_l}(\hat{\mathbf{p}})\right), \tag{57}$$

and depend on the direction of the incident electron beam $\hat{\mathbf{p}}$.

We now derive the total cross section from Eq. (53). Averaging Eq. (53) with respect to the directions of the incident and scattered electron $\hat{\mathbf{p}}$ and $\hat{\mathbf{p}}'$ gives

$$\bar{\sigma}(i'\leftarrow i)=\frac{4\pi^3}{p^2}\sum_{LL'}\langle L',i'|t|L,i\rangle\langle L,i|t^\dagger|L',i'\rangle. \tag{58}$$

Again we convert the states $|L,i\rangle$ into our symmetry-adapted functions, and averaging over target spins we obtain

$$\bar{\sigma}(i'\leftarrow i)=\frac{4\pi^3}{p^2}\sum_{PS}\sum_{p_2p'_2hh'll'}\frac{N_P(2S+1)}{2N_i(2S_i+1)}$$
$$\times|\langle\tilde{\bar{\Phi}}^{\tilde{\Gamma}}_{i'p'_1p'_2h'l'}|t|\tilde{\bar{\Phi}}^{\tilde{\Gamma}}_{ip_1p_2hl}\rangle|^2, \tag{59}$$

where $\tilde{\Gamma}\equiv\{PS\Pi\}$. Here p is the magnitude of the momentum of the incident electron. P, p_1, and p_2 represent the cubic symmetries of the compound state, the target, and the scattering electron, respectively. The scattering electron has angular momentum l, and the h indicates that different p_2's may be associated with each value of l. N_i and N_P are the degeneracies of the target state and the compound state, and the S_i and S are the corresponding spins.

VI. RESULTS

To obtain convergence in our results (to within 1% accuracy), it is sufficient to use 15 one-electron functions u_j in Eq. (26). We take the angular momentum of the scattered electron up to $l=4$, sufficient for convergence in the inelastic scattering cross section throughout the energy range that we consider, though not for the elastic scattering cross section.

A. Total cross section

We first consider the total scattering cross section to study the variation in intensity with the energy of the incident electron $E_{\rm inc}=p^2/2$. Figure 1 shows results for the elastic cross section and Fig. 2 two representative inelastic cross sections. The elastic cross section is seen to be 2–3 orders of magnitude larger than the inelastic cross sections, in agreement with LE-EELS experiments where the low-energy region of the spectra is dominated by the zero-loss peak.[3] Unlike the inelastic cross sections, the elastic cross section has not converged as a function of l for energies greater than about 0.8 a.u. Figure 1 gives the contributions to the cross section from different l values [the contributions in Eq. (59) from $l\neq l'$ are very small], and we see that these show resonance (and antiresonance) structure increasing in energy as l increases. The higher-l values hardly contribute at lower energies.

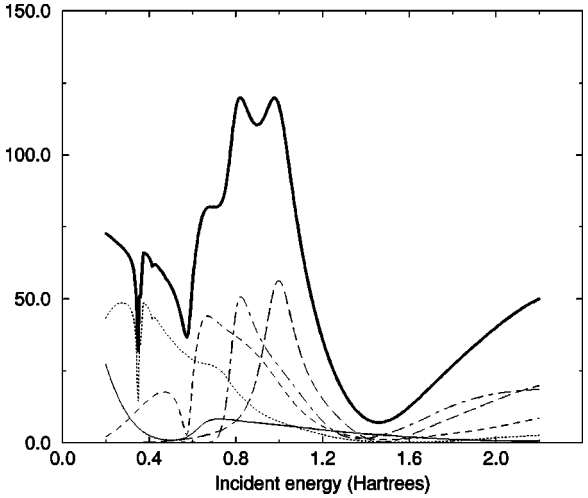

FIG. 1. The total elastic cross section (thick solid line) together with the individual contributions from the orbital angular momentum components of the scattering electron, $l=0$ (thin solid line), $l=1$ (dotted line), $l=2$ (dashed line), $l=3$ (dot-dashed line), and $l=4$ (long-dashed line). The y axis has units a_0^2.

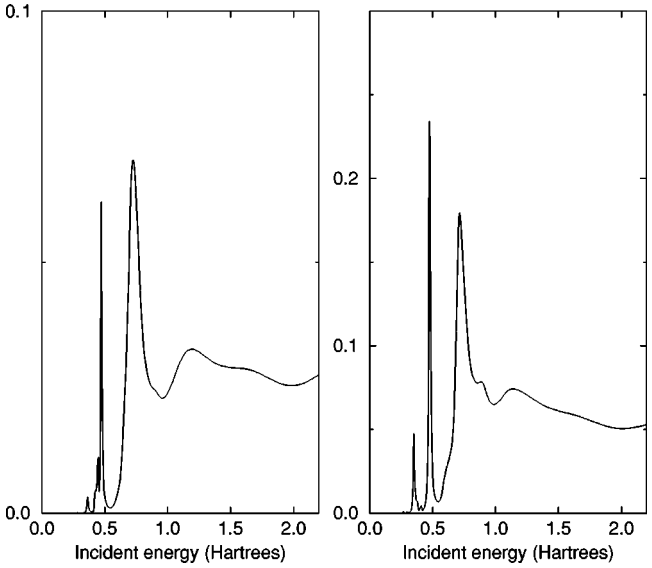

FIG. 2. The averaged total cross sections for the loss processes ${}^3A_{2g}\rightarrow{}^1T_{1g}$ (3.28 eV), and ${}^3A_{2g}\rightarrow{}^3T_{1g}$ (3.13 eV). The y axis has units a_0^2.

All the inelastic cross sections show very sharp resonance structure at energies below 0.8 a.u., whereas above this value the spectra are fairly featureless and very similar. These resonances occur due to coupling between the different orbital angular momentum components of the scattering electron and the Ni $3d$ target, as we can see from Fig. 3, which shows the angular momentum decomposition. Such resonances also appear in the free ion, and the couplings are to both the initial and final target states. We note in Fig. 3 that the inelastic results are indeed converged for $l=4$.

In general, the triplet-triplet excitations that involve both direct and exchange scattering mechanisms are more intense

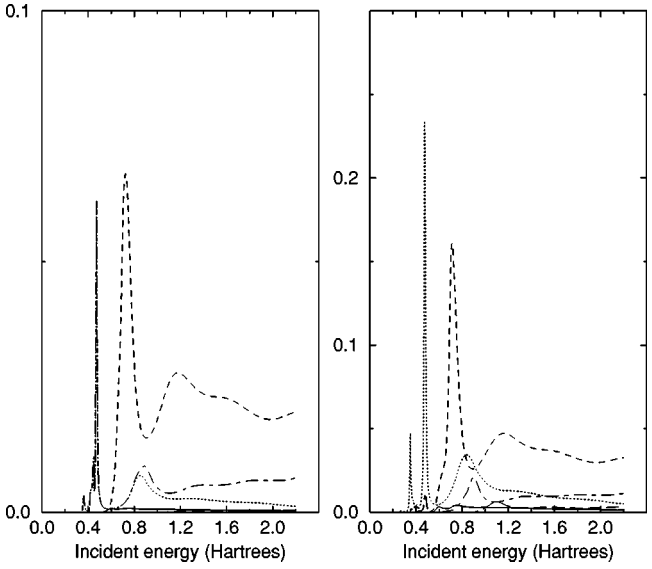

FIG. 3. The contributions from the orbital angular momentum components of the scattering electron to the total cross sections for the loss processes ${}^3A_{2g}\rightarrow{}^1T_{1g}$ (3.28 eV) and ${}^3A_{2g}\rightarrow{}^3T_{1g}$ (3.13 eV). The overall total cross sections are omitted to avoid confusion with the various lines, but are given in Fig. 2. The lines are defined as in Fig. 1, and the y axis again has units a_0^2.

than the multiplicity-changing triplet-singlet excitations that only occur via exchange scattering. Surprisingly, the cross sections for the multiplicity-changing excitations stay significant for energies much greater than the loss energies. In electron scattering from simple atoms (such as He), the scattering cross section is largest when the primary energy is almost equal to the loss energy and negligible when the ratio of primary energy to loss energy is greater than about 10.[26] Experimental measurements confirm that exchange scattering of the $3d$ excitations in NiO play an important role at these higher primary energies, and this had been attributed to hybridization of the localized states with bandlike states.[3] However, our model does not include these hybridization effects and yet we still observe the contribution of exchange scattering.

Among the triplet-singlet transitions the weakest are those from the ${}^3A_{2g}$ ground state to the states ${}^1A_{1g}$, ${}^1E_g$, and ${}^1T_{2g}$, and the weakest of the triplet-triplet transitions is to the ${}^3T_{1g}$ state. The ${}^3A_{2g}$ ground state has the electronic configuration $(t_{2g})^6(e_g)^2$ (i.e., 2 holes in e_g),[3] thus we can rearrange the hole configuration and calculate the states produced from each rearrangement using the symmetry of the system and group theoretical direct product techniques. From these it is found that these weakest transitions in both the triplet-singlet and triplet-triplet cases occur when there are two holes in t_{2g}, i.e., the $(t_{2g})^4(e_g)^4$ electron configuration. This is reasonable as two electrons need to be excited in order to produce the latter configuration.

B. Differential cross section: Angle dependence

We now consider the differential cross section, with the incoming and outgoing electron beams in one scattering plane in order to study spatial symmetry. In all the following studies the incident and scattering beams are in the plane containing the surface normal (001) and the (100) axis. θ_i and θ_f are measured with respect to the surface normal, and ϕ is the azimuthal angle measured with respect to the (100) axis.

Figure 4 shows a polar plot for the spin-averaged differential cross-section of the elastic peak at $E_{\rm inc}=20$ eV. This is dominated by forward scattering, as we might expect. In a multiple-scattering treatment of inelastic scattering, an inelastic-scattering event is sandwiched between multiple-elastic-scattering events: the dominance of forward elastic scattering means that the directions of the incoming and inelastically scattered electron will tend to be preserved, and our single-scattering treatment is better justified.

The polar plots given in Figs. 5–8 show the spin-averaged differential cross sections for several inelastic transitions, for an incident energy of 20 eV. As we can see, the transitions to the states ${}^1A_{1g}$ and ${}^3T_{2g}$ (Figs. 5 and 6, respectively) show zero intensity for forward and backward scattering. We see from the shape of the electron scattering that the excitations in Figs. 5 and 6 are dominated by d-wave scattering, whereas in Figs. 7 and 8 there is a small contribution from p waves in addition to the dominant d-wave scattering. Figure 9 shows the differential cross sections for excitations to the different T_{1g} states, which we see have a similar angle dependence. This emphasizes the importance of the symmetry of the target state in determining the angular distribution of scattering.

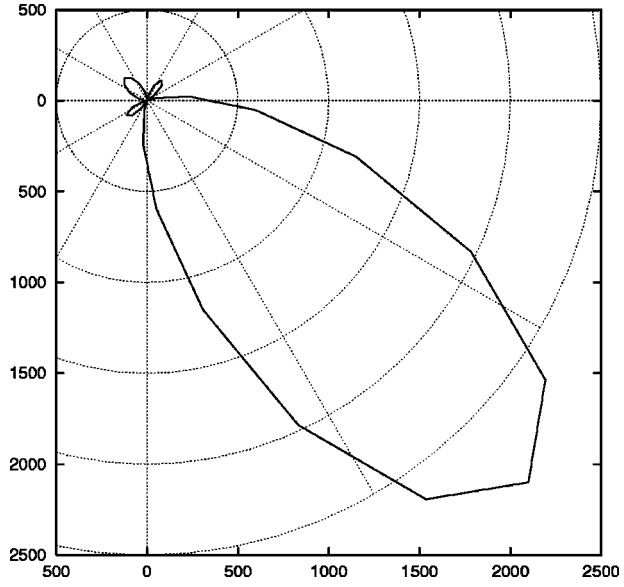

FIG. 4. Polar plot of the spin-averaged differential cross section for the elastic transition ${}^3A_{2g} \rightarrow {}^3A_{2g}$. The axes have units a_0^2. $E_{\mathrm{inc}} = 20$ eV.

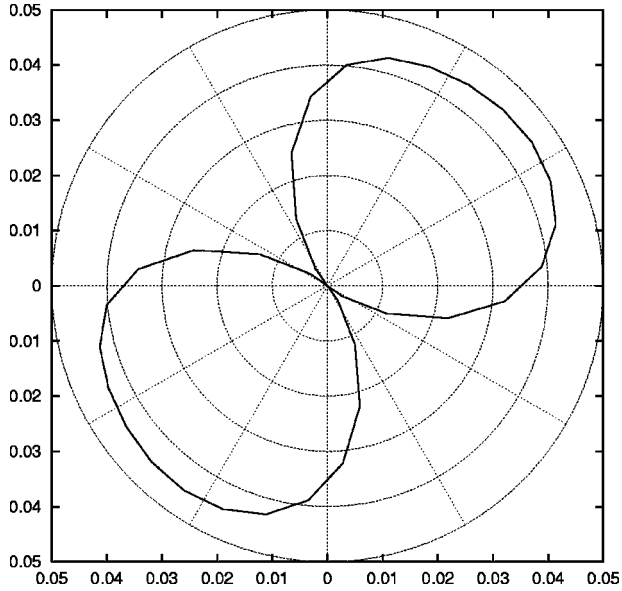

FIG. 6. Polar plot of the spin-averaged differential cross-sections of transition to final state ${}^3T_{2g}$ (1.05 eV). The axes have units a_0^2. $E_{\mathrm{inc}} = 20$ eV.

When the incoming and outgoing electron beams lie parallel to a particular symmetry axis or in a particular mirror plane, there are often geometries for which the cross section must be zero by the point group symmetry. In this way we can explain the results shown in Figs. 5 and 6, with zero intensity for forward and backward scattering in the transitions to A_{1g} and T_{2g} multiplet states. This can be seen from the transformation properties of the initial and final states,[14,12] and the corresponding matrix elements. In the case of the transitions to A_{1g} we consider the matrix element $\langle \mathbf{p}' A_{1g} | T | \mathbf{p} A_{2g} \rangle$, where $\mathbf{p}$ and $\mathbf{p}'$ label the incident and outgoing electron beams. When $\mathbf{p}$ and $\mathbf{p}'$ are both parallel to the $(\bar{1}01)$ axis, we consider the twofold rotation about this axis. A_{2g} changes sign, but A_{1g} is invariant—hence the matrix element, which must be invariant under the transformation, is zero. This is consistent with a previous Letter.[27]

A similar argument holds for the transition to the T_{2g} states, where the matrix element under consideration is $\langle \mathbf{p}' T_{2g} | T | \mathbf{p} A_{2g} \rangle$. However, T_{2g} has three components that transform as xy, yz, and zx, so a more detailed analysis is necessary by investigating each component individually. Again considering the twofold rotation about the $(\bar{1}01)$ symmetry axis, the zx component displays no change in sign, which along with the sign change of the A_{2g} state means that the matrix element must be zero. However, the two remaining components of the T_{2g} state transform into each other so

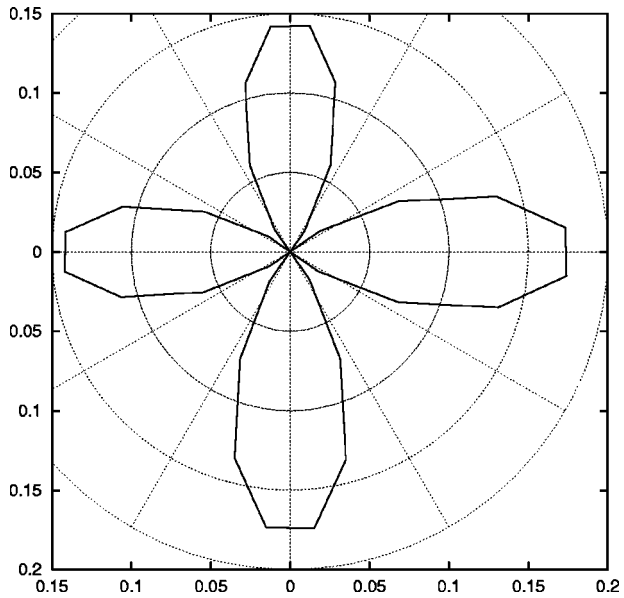

FIG. 5. Polar plot of the spin-averaged differential cross-sections of transition to final state ${}^1A_{1g}$ (2.80 eV). The axes have units a_0^2. $E_{\mathrm{inc}} = 20$ eV.

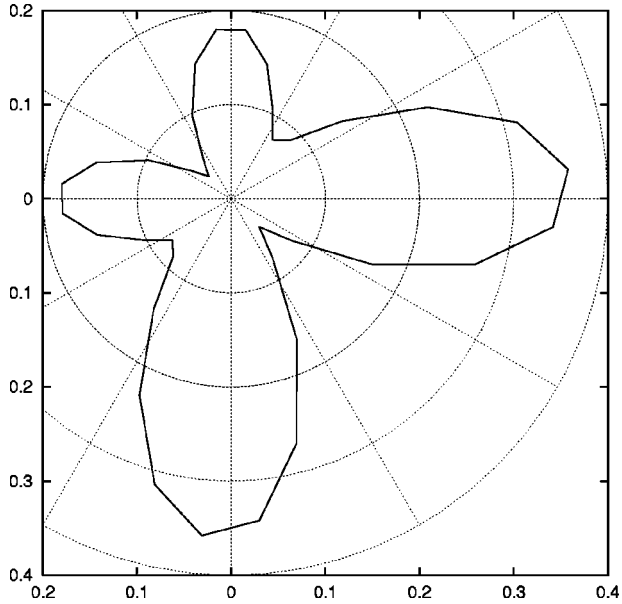

FIG. 7. Polar plot of the spin-averaged differential cross sections of transition to final state ${}^1E_g$ (1.70 eV). The axes have units a_0^2. $E_{\mathrm{inc}} = 20$ eV.

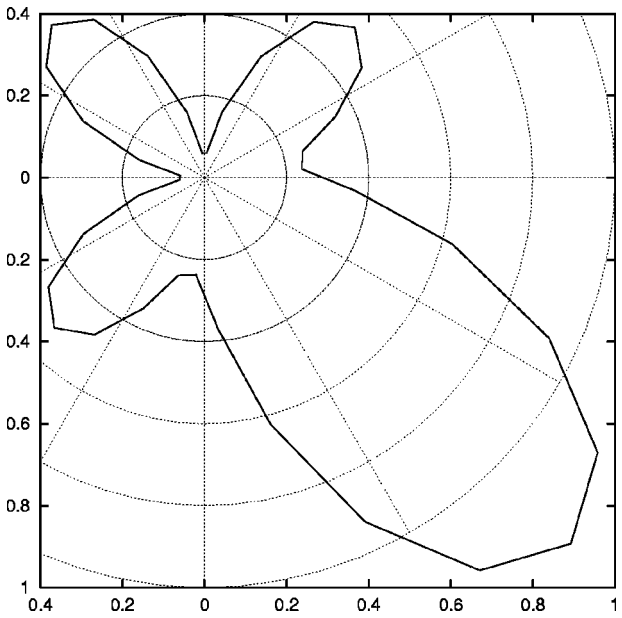

FIG. 8. Polar plot of the spin-averaged differential cross sections of transition to final state $^3T_{1g}$ (3.13 eV). The axes have units a_0^2. $E_{\rm inc}=20$ eV.

nothing can be inferred for these. In order to examine these we apply a reflection in the z-x mirror plane. Now the A_{2g} state is invariant under such a reflection, but xy and yz display a change in sign. So the corresponding matrix elements must also be zero. So we have shown that an excitation to the T_{2g} state shows zero intensity for backward and forward scattering by a combination of rotation and mirror-plane arguments.

There seems to be no symmetry reason for the zeros at $\pm 90°$ in the transition to $^1A_{1g}$ in Fig. 5. These are presumably a consequence of the partial waves of the scattering electron that couple to this transition.

C. Differential cross section: Spin dependence

Spin-resolved experiments, in which the spins of the incident and scattered electrons are determined, add another variable to the description of scattering. There are interesting rules relating the intensities of varying spin flip, which follow from the properties of the Clebsch-Gordan coefficients $(SM_S|S_iM_{S_i}\frac{1}{2}m)$ in Eq. (56). Only certain combinations of Clebsch-Gordan coefficients are nonvanishing. Considering the multiplicity-changing transitions, we find that for the non-spin-flip transitions the only nonvanishing combination is $(\frac{1}{2}\frac{1}{2}|10\frac{1}{2}\frac{1}{2})^2(\frac{1}{2}\frac{1}{2}|00\frac{1}{2}\frac{1}{2})^2$, which reduces to $\frac{1}{3}$. Similarly the only nonvanishing combination for the spin-flip transition is $(\frac{1}{2}-\frac{1}{2}|1-1\frac{1}{2}\frac{1}{2})^2(\frac{1}{2}-\frac{1}{2}|00\frac{1}{2}-\frac{1}{2})^2$, which equals $\frac{2}{3}$. Therefore the spin-flip to non-spin-flip ratio is 2, as found in a previous Letter.[27] This combination only holds for the triplet-singlet transitions; the triplet-triplet transitions have a more complicated spin-flip to non-spin-flip ratio that needs to be calculated explicitly.

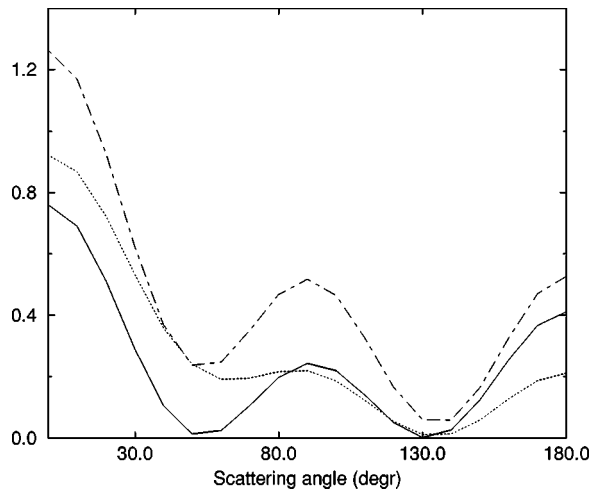

FIG. 9. The spin-averaged differential cross sections for excitations to final states with T_{1g} symmetry. The loss energies are 3.28 eV ($^1T_{1g}$, solid line), 3.13 eV ($^3T_{1g}$, dot-dashed line) and 1.75 eV ($^3T_{1g}$, dotted line). The y axis has units a_0^2. $E_{\rm inc}=20$ eV.

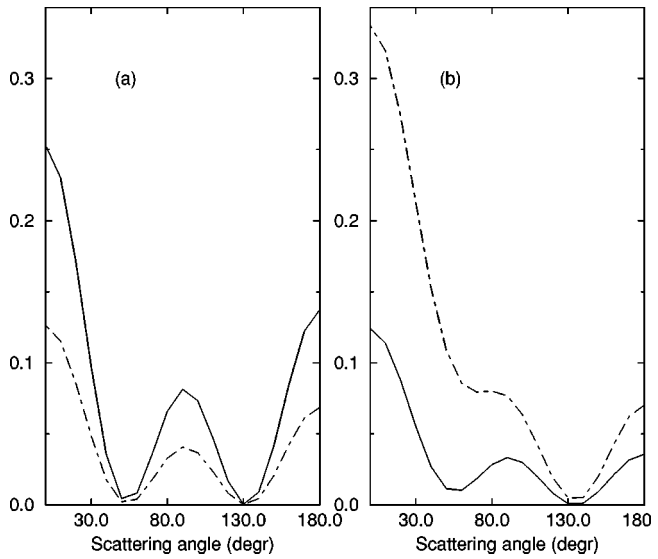

FIG. 10. The spin-flip (solid line) and non-spin-flip (dot-dashed line) differential cross sections for two transitions: (a) $^3A_{2g}\rightarrow{}^1T_{1g}$ (3.28 eV energy loss) and (b) $^3A_{2g}\rightarrow{}^3T_{1g}$ (1.75 eV energy loss). The scattering angle is related to the polar angle θ_f by $\theta_f=135°-\alpha$. The y axis has units a_0^2. $E_{\rm inc}=20$ eV.

Figure 10 shows the intensity of both the spin-flip and non-spin-flip contributions for the two transitions indicated. The incoming scattering angles are fixed with $\theta_i=45°$ and $\phi_i=0°$. The outgoing scattering angle α is varied, with fixed $\phi_f=180°$. The incident energy of the scattering electron is 20 eV. Figure 10(a) shows a multiplicity-changing transition, and the spin-flip to non-spin-flip ratio is 2 in agreement with the analysis of the Clebsch-Gordan coefficients. In the triplet-triplet transition shown in Fig. 10(b), the spin-flip to non-spin-flip ratio changes with scattering angle, and the non-spin-flip contribution is stronger than the spin-flip contribution.

VII. COMPARISON WITH EXPERIMENT

For a comparison with experimental results we now consider the differential scattering cross sections, and we first average over spins of the target and scattering electron for both incident and outgoing cases, corresponding to spin-integrated LE-EELS experiments. Figure 11 shows results calculated from our model for two incident energies and two

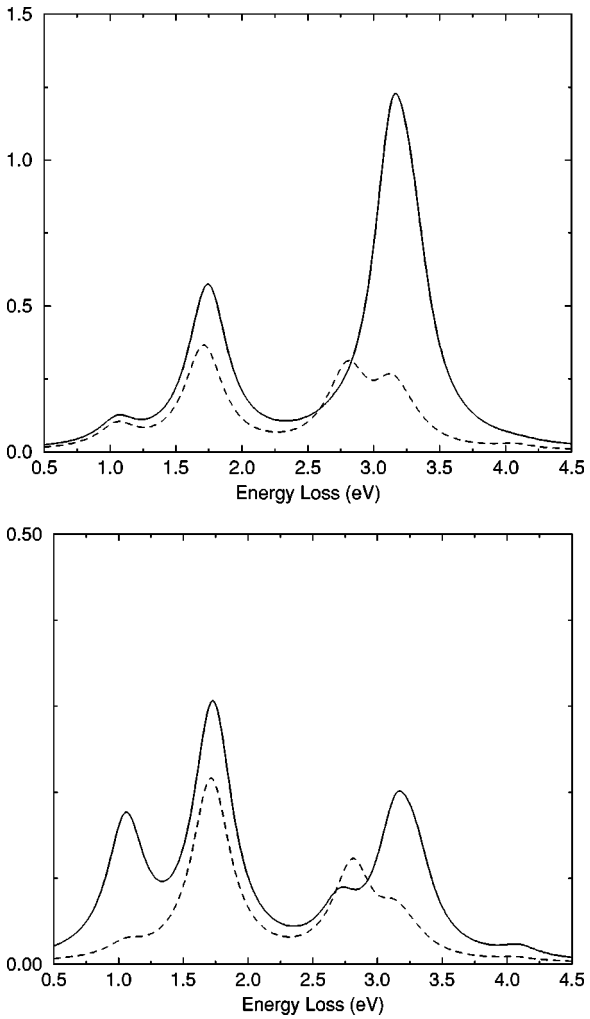

FIG. 11. The spin-averaged differential cross sections of two scattering geometries and two incident electron energies. The upper plot has $E_{\rm inc}=20$ eV and the lower has $E_{\rm inc}=50$ eV. The solid line represents specular scattering geometry ($\theta_i=\theta_f=45°$) and the dashed line off-specular scattering ($\theta_i=45°, \theta_f=10°$). Angles are measured with respect to the surface normal and the *y* axis has units a_0^2.

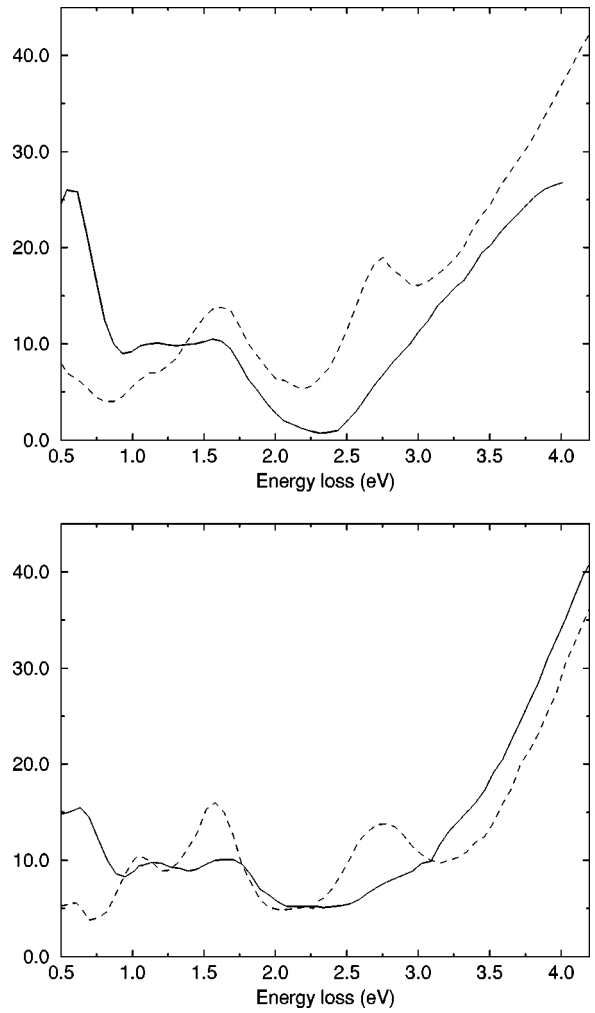

FIG. 12. Experimental spectra from Gorschlüter and Merz. The *y* axis is in arbitrary units; otherwise the definitions are as in Fig. 11.

scattering geometries, which are indicated. In each case $\phi_i=0°$ and $\phi_f=180°$, where ϕ is the azimuthal angle measured with respect to the (100) axis. The discrete losses are broadened by a Lorentzian of 250 meV width for comparison with experiment. These plots are compared with experimental data from Gorschlüter and Merz,[3] given in Fig. 12. In our model we ignore the dominant elastic peak, and we do not consider the 0.6 eV loss peak as it is due to a surface excitation. Charge transfer excitations across the band gap (above about 4 eV) are also excluded in our atomic model.

From the two figures it is evident that the cross sections are heavily dependent on the polar angles of the incident and outgoing electron beams, as we discussed in detail in Sec. VI B. The relative peak intensities show good agreement with the experimental data. The 1.05 eV loss peak is due to a single transition to ${}^3T_{2g}$. The big peak at 1.7 eV is due to two overlapping transitions, ${}^1E_g$ (1.70 eV) and ${}^3T_{1g}$ (1.75 eV). Similarly, the 3.2 eV peak is due to two overlapping transitions, ${}^3T_{1g}$ (3.13 eV) and ${}^1T_{1g}$ (3.28 eV). This peak appears to be too large but this is due to the loss peaks being closer together in our calculations than in experiments, where the ${}^3T_{1g}$ peak occurs at 3.0 eV and the ${}^1T_{1g}$ peak at 3.55 eV. When the discrete losses are broadened by the Lorentzian, the peaks that are close together produce a very large combined peak, whereas their greater separation in experiment leads to a smaller peak that is submerged in the charge transfer excitations across the band gap.

We now fix the incoming electron spin (spin up) and select the outgoing electron spin, corresponding to spin-polarized experiments. Figure 13 shows our spin-flip spectra for varying scattering angles α in the range $73°\leqslant\alpha\leqslant123°$, with an interval of 3.125°. (The scattering angle is related to θ_f by $\theta_f=135°-\alpha$.) The incident energy is 33 eV and the incident angle fixed at 45°. These results, which are Lorentzian broadened by 175 meV, can be compared with the experimental spin-flip data from Müller *et al.*[6] given in Fig. 14. Again we ignore the elastic peak and do not consider the 0.6 eV surface excitation. The loss peak at 3.2 eV appears to be too narrow due to the proximity of the two contributing states as explained earlier. Our model shows reasonable agreement with experiment. The peak at 3.2 eV, albeit too narrow, dramatically drops off at large α, apparently in agreement with experiment (the role of charge transfer excitations are unclear). Most significantly, at 2.7 eV we see a

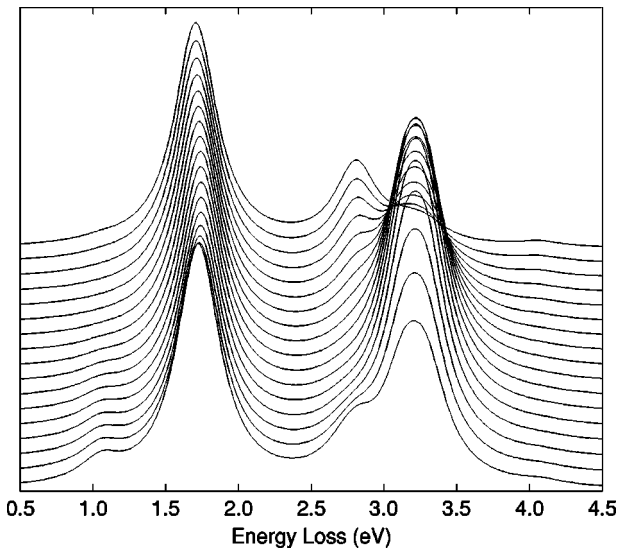

FIG. 13. Spin-flip spectra for a range of scattering angles $73° \leqslant \alpha \leqslant 123°$ in intervals of 3.125° with 73° being the lowest line. The remaining polar angles were fixed with $\theta_i = 45°$, $\phi_i = 0°$, and $\phi_f = 180°$, $E_{\text{inc}} = 33$ eV.

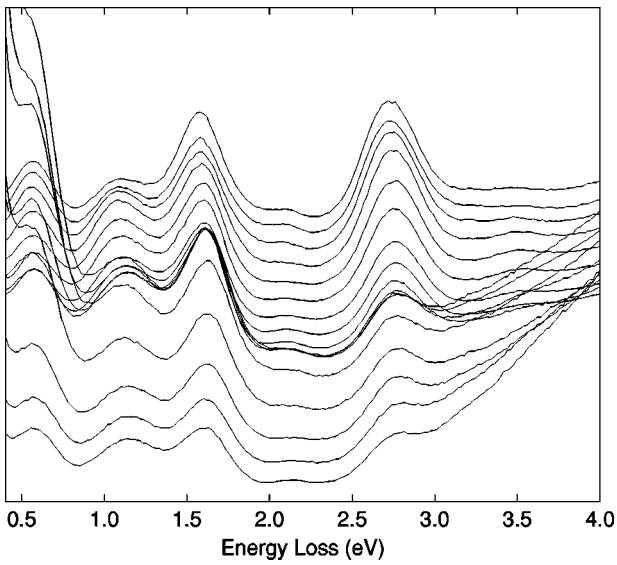

FIG. 14. Spin-flip experimental data where the scattering angle is varied ($73° \leqslant \alpha \leqslant 123°$).

small shoulder at 73° that slowly increases and becomes quite dominant at 123°. This peak is of particular interest as it is a combination of two triplet-singlet excitations to the states ${}^1A_{1g}$ (2.80 eV) and ${}^1T_{2g}$ (2.70 eV), for which spin-flip dominates (Sec. VI C). There is remarkable agreement between our model and experiment for this peak.

VIII. MULTIPLE SCATTERING

Although we can make contact with experiment using the single-scattering approximation, a full theory of LE-EELS must treat the multiple-elastic-scattering events that occur before and after the inelastic scattering. To do this we take results from the theory[28,29] of diffuse LEED used to treat the effect of an additional scatterer, with the further simplification that the cross section for inelastic scattering is so low compared with elastic that we need only consider a single inelastic scattering, with no multiple events.

If t is the t matrix for inelastic scattering by a particular Ni^{2+} ion in isolation, and T is for elastic scattering by the whole semi-infinite crystal (including this ion), the full inelastic t matrix for the ion to undergo the transition in the crystal environment is given by

$$T_{\text{in}} = t + tG_0T + TG_0t + TG_0tG_0T. \tag{60}$$

Here G_0 is the free-electron propagator. This can be simplified to

$$T_{\text{in}} = (1 + TG_0)t(1 + G_0T). \tag{61}$$

The transition amplitude for plane wave $\mathbf{p}$ to be scattered into $\mathbf{p}'$, with the target undergoing the transition from i to i', is then given by

$$\langle \mathbf{p}', i' | T_{\text{in}} | \mathbf{p}, i \rangle = \langle \mathbf{p}'(1 + TG_0), i' | t | (1 + G_0T)\mathbf{p}, i \rangle. \tag{62}$$

We can consider this as a transition on the target ion between $\psi^+_{\mathbf{p}} = (1 + G_0T)|\mathbf{p}\rangle$ and $\psi^-_{\mathbf{p}'} = (1 + G_0^\dagger T^\dagger)|\mathbf{p}'\rangle$. $\psi^+_{\mathbf{p}}$ is the LEED wave function arising from scattering $\exp(i\mathbf{p}\cdot\mathbf{r})$ off the surface elastically. $\psi^-_{\mathbf{p}'}$ is the time-reversed LEED wave function corresponding to $\exp(i\mathbf{p}'\cdot\mathbf{r})$: we let $\exp(-i\mathbf{p}\cdot\mathbf{r})$ scatter off the surface, and then take the complex conjugate. The transition between these states is caused by t. The inelastic scattering from different Ni^{2+} ions adds incoherently—we average the intensity from different depths of ions.

In this multiple-scattering formalism it is also possible to include the damping of the propagating electrons due to mean-free-path effects in the electron gas. These are due to the excitation of electron-hole pairs and plasmons, and the effect on the free-electron wave propagating between our localized scattering events can be described by a complex optical potential ''felt'' by G_0. This is exactly the same as in conventional LEED or photoemission theory.[30,31] This damping is necessary to account for the surface sensitivity of LE-EELS. The inclusion of multiple scattering in this way is our next aim in describing LE-EELS from NiO and other transition-metal oxides and will be the subject of future work.

ACKNOWLEDGMENTS

We wish to thank Dr. M. Boon for his help with the group theoretical aspects in this paper. P. Jones received financial support from EPSRC.

[1] J. C. Fuggle and J. E. Inglesfield, in *Unoccupied Electronic States*, edited by J. C. Fuggle and J. E. Inglesfield (Springer-Verlag, Berlin, 1992).
[2] J. Fink, in *Unoccupied Electronic States*, edited by J. C. Fuggle and J. E. Inglesfield (Springer-Verlag, Berlin, 1992).
[3] A. Gorschlüter and H. Merz, Phys. Rev. B **49**, 17 293 (1994).
[4] J. J. M. Michiels, J. E. Inglesfield, C. J. Noble, V. M. Burke, and P. G. Burke, Phys. Rev. Lett. **78**, 14 (1997).
[5] P. G. Burke and K. A. Berrington, *Atomic and Molecular Processes: An R-matrix Approach* (Institute of Physics Publishing, Bristol, 1993).
[6] F. Müller, P. Steiner, Th. Straub, D. Reinicke, S. Palm, R. de Masi, and S. Hüfner, Surf. Sci. **442**, 485 (1999).
[7] D. C. S. Allison, P. G. Burke, and W. D. Robb, J. Phys. B **5**, 55 (1971).
[8] P. G. Burke and K. T. Taylor, J. Phys. B **8**, 2620 (1975).
[9] C. Bloch, Nucl. Phys. **4**, 503 (1957).
[10] A. M. Lane and D. Robson, Phys. Rev. **151**, 774 (1966).
[11] J. R. Taylor, *Scattering Theory* (Wiley, New York, 1972).
[12] S. Sugano, Y. Tanabe, and H. Kamimura, *Multiplets of Transition-Metal Ions in Crystals* (Academic Press, New York, 1970).
[13] H. Ibach and H. Lüth, *Solid-State Physics* (Springer-Verlag, Berlin, 1991).
[14] M. Tinkham, *Group Theory in Quantum Mechanics* (McGraw-Hill, New York, 1964).
[15] C. J. Bradley and A. P. Cracknell, *Mathematical Theory of Symmetry in Solids* (Clarendon Press, Oxford, 1972).
[16] M. Boon (private communication).
[17] A. Fujimori and F. Minami, Phys. Rev. B **30**, 957 (1984).
[18] D. W. Lynch and R. D. Cowan, Phys. Rev. B **36**, 9228 (1987).
[19] P. G. Burke, V. M. Burke, and K. M. Dunseath, J. Phys. B **27**, 5341 (1994).
[20] P. J. A. Buttle, Phys. Rev. **160**, 719 (1967).
[21] A. Gonis, *Green Functions for Ordered and Disordered Systems* (North-Holland, Amsterdam, 1992).
[22] R. E. Palmer and P. J. Rous, Rev. Mod. Phys. **64**, 383 (1992).
[23] K. Terakura, T. Oguchi, A. R. Williams, and J. Kübler, Phys. Rev. B **30**, 4734 (1984).
[24] K. L. Baluja, P. G. Burke, and L. A. Morgan, Comput. Phys. Commun. **27**, 299 (1982).
[25] J. C. Slater, *The Self-Consistent Field for Molecules and Solids* (McGraw-Hill, New York, 1974), Vol. 4.
[26] G. F. Hanne, Phys. Rep. **95**, 95 (1983).
[27] J. J. M. Michiels, J. E. Inglesfield, C. J. Noble, V. M. Burke, and P. G. Burke, J. Phys.: Condens. Matter **9**, L543 (1997).
[28] J. B. Pendry and D. K. Saldin, Surf. Sci. **145**, 33 (1984).
[29] D. K. Saldin, J. B. Pendry, M. A. Van Hove, and G. A. Somorjai, Phys. Rev. B **31**, 1216 (1985).
[30] J. C. Inkson, Surf. Sci. **28**, 69 (1971).
[31] L. Hedin, J. J. M. Michiels, and J. E. Inglesfield, Phys. Rev. B **58**, 15 565 (1998).